East Tennessee State University

Digital Commons @ East Tennessee State University

8-9-2017

On the Binary Nature of Massive Blue Hypergiants: High-resolution X-Ray Spectroscopy Suggests That Cyg OB2 12 is a Colliding Wind Binary - IOPscience

Lidia M. Oskinova
University of Postdam

David P. Huenemoerder
Massachusetts Institute of Technology

Wolf-Rainer Hamann
University of Potsdamn

Tomer Shenar
University of Potsdam

A. A.C. Sander
University of Potsdam

See next page for additional authors

Follow this and additional works at: https://dc.etsu.edu/etsu-works

Part of the Stars, Interstellar Medium and the Galaxy Commons

Citation Information

On the Binary Nature of Massive Blue Hypergiants: High-resolution X-Ray Spectroscopy Suggests That Cyg OB2 12 is a Colliding Wind Binary - IOPscience

Copyright Statement

Creator(s)

Lidia M. Oskinova, David P. Huenemoerder, Wolf-Rainer Hamann, Tomer Shenar, A. A.C. Sander, Richard Ignace, H. Todt, and R. Hainich

On the Binary Nature of Massive Blue Hypergiants: High-resolution X-Ray Spectroscopy Suggests That Cyg OB2 12 is a Colliding Wind Binary

L. M. Oskinova[1], D. P. Huenemoerder[2] , W.-R. Hamann[1], T. Shenar[1] , A. A. C. Sander[1],
R. Ignace[3] , H. Todt[1], and R. Hainich[1]
[1] Institute for Physics and Astronomy, University Potsdam, D-14476 Potsdam, Germany; lida@astro.physik.uni-potsdam.de
[2] Massachusetts Institute of Technology, Kavli Institute for Astrophysics and Space Research, 70 Vassar St., Cambridge, MA 02139, USA
[3] Department of Physics and Astronomy, East Tennessee State University, Johnson City, TN 37663, USA

Abstract

The blue hypergiant Cyg OB2 12 (B3Ia$^+$) is a representative member of the class of very massive stars in a poorly understood evolutionary stage. We obtained its high-resolution X-ray spectrum using the *Chandra* observatory. PoWR model atmospheres were calculated to provide realistic wind opacities and to establish the wind density structure. We find that collisional de-excitation is the dominant mechanism depopulating the metastable upper levels of the forbidden lines of the He-like ions Si XIV and Mg XII. Comparison between the model and observations reveals that X-ray emission is produced in a dense plasma, which could reside only at the photosphere or in a colliding wind zone between binary components. The observed X-ray spectra are well-fitted by thermal plasma models, with average temperatures in excess of 10 MK. The wind speed in Cyg OB2 12 is not high enough to power such high temperatures, but the collision of two winds in a binary system can be sufficient. We used archival data to investigate the X-ray properties of other blue hypergiants. In general, stars of this class are not detected as X-ray sources. We suggest that our new *Chandra* observations of Cyg OB2 12 can be best explained if Cyg OB2 12 is a colliding wind binary possessing a late O-type companion. This makes Cyg OB2 12 only the second binary system among the 16 known Galactic hypergiants. This low binary fraction indicates that the blue hypergiants are likely products of massive binary evolution during which they either accreted a significant amount of mass or already merged with their companions.

Key words: stars: individual (Cyg OB2 12) – stars: massive – stars: mass-loss – stars: winds, outflows – supergiants – X-rays: stars

1. Introduction

Only a small number of stars have established masses in excess of 100 $M_\odot$. Though such heavy-weights are rare, their formation, evolution, and deaths are of significant interest.

Very massive stars have the highest bolometric luminosities among all stellar types, and are often located above the empiric Humphreys–Davidson limit that restricts the domain of stable stars (Humphreys & Davidson 1979) in the Hertzsprung-Russell diagram (HRD). Their extremely large luminosities allow us to observe them at large distances as well as in heavily obscured regions (Barniske et al. 2008; Crowther et al. 2010).

Very massive stars display a rich variety of phenomena (e.g., luminous blue variables, LBVs) and populate various spectral types. Among them are late-type nitrogen-sequence Wolf-Rayet stars (WNh), Of/WNL transition type stars, and the blue hypergiants with luminosity class Ia$^+$. The latter class is the subject of this study. The evolutionary relationship between various types of very massive stars is not yet established, despite large theoretical efforts (e.g., Sanyal et al. 2015).

Mass-loss plays a major role in determining the evolutionary path of very massive stars. These stars may lose matter via three mechanisms. First, matter can be lost via line-driven winds, as is ubiquitous for all hot massive stars (e.g., Gräfener & Hamann 2005). Alternatively, mass can be lost via super-Eddington winds or LBV eruptions (Shaviv 2000; Quataert et al. 2016). In binary systems, finally, mass transfer may occur that significantly affects the evolution (Vanbeveren et al. 1998; Langer 2012). Which of these mechanisms is most important in the lives of blue hypergiants is not yet clear.

In the present paper we employ X-ray observations to investigate the nature of one of the most massive and luminous stars in the Milky Way, Cyg OB2 12 (HIP 101364, VI Cyg 12, Schulte 12). Over the last decade, X-rays have become an established diagnostic tool to probe massive stars (Oskinova 2016, and references therein).

Radiatively driven winds of early-type stars are typically fast ($v_\infty > 1000$ km s^{-1}) and intrinsically unstable (Lucy & White 1980; Feldmeier et al. 1997). In the winds from OB-type supergiants, hydrodynamical instabilities lead to strong shocks where some fraction of the wind is heated to a few million Kelvin. The X-ray luminosity of these stars correlates with their bolometric luminosity as $L_X \propto 10^{-7} L_{bol}$ (Pallavicini et al. 1981). The X-ray spectra of OB stars are thermal. The hottest plasma is generated in the inner wind regions, and the X-ray lines are broad and often blueshifted (Oskinova et al. 2006; Waldron & Cassinelli 2007; Hervé et al. 2013; Puebla et al. 2016). The X-ray luminosity displays slow variability on the timescale of days and on the level of a few tens of percent (Oskinova et al. 2001; Ignace et al. 2013; Nazé et al. 2013; Massa et al. 2014). In stars with very dense winds, such as, e.g., Wolf-Rayet (WR) stars, X-rays may be produced by the interaction of the fast wind flow with slower wind structures far out in the wind (Oskinova et al. 2012; Gayley 2016). This mechanism is manifested by broad and blueshifted X-ray line profiles and associated plasma temperatures of $\gtrsim$10 MK (Huenemoerder et al. 2015).

The majority of massive stars are found in binary or multiple systems (e.g., Chini et al. 2012; Sana et al. 2012). In such systems, the winds of the components may collide, leading to the emission of X-rays from the wind collision zone (e.g.,

Pittard 2009). The X-ray signatures of colliding wind binaries are well-established (Rauw & Nazé 2016). The plasma temperature is often higher than that measured from the X-ray spectra of single stars. Colliding wind X-ray spectra may show signs that the plasma departs from collisional ionization equilibrium (Pollock et al. 2005). The X-ray line profiles may display a variety of shapes (Henley et al. 2005). The X-ray light curves of colliding wind binaries typically show orbital variability.

However, not all hot massive stars are detectable X-ray sources, e.g., single metal-enriched WR stars with spectral types WO and WC are quite weak in X-rays (Oskinova et al. 2009; Rauw et al. 2015). Single LBVs are also weak X-ray sources. The winds of these stars are slow (a few $\times 100$ km s^{-1}) and dense ($\dot{M} = 10^{-3}$ ... 10^{-6} $M_\odot$ yr^{-1}) (e.g., Hillier et al. 2001). The radiative driving instabilities and associated shocks, likely do not develop in these winds. Moreover, the high wind density makes it especially difficult for the X-rays to escape. The lack of X-ray emission is observationally established for the majority of LBVs. All LBVs that have been found to be X-ray-bright are colliding wind systems (Oskinova 2005; Nazé et al. 2012).

In this paper we investigate the nature of the X-ray emission of Cyg OB2 12 by means of high-resolution X-ray spectroscopy. The object of our study is introduced more fully in Section 2. The *Chandra* X-ray spectrum is addressed in Section 3, and the conclusions from our study are presented in Section 4.

2. Cyg OB2 12

Cyg OB2 12 is among the most massive Galactic blue hypergiants known. This star is a likely member of the Cyg OB2 association. In agreement with Clark et al. (2012), we adopt a distance of 1.75 kpc throughout this work. Cyg OB2 12 suffers significant reddening ($A_V \approx 10$ mag). Part of this high extinction could be due to circumstellar matter that might have been lost over the evolution of this very massive star. Maryeva et al. (2016) suggested that such a circumstellar shell could absorb up to 1 mag in the *V*-band. Whittet (2015) pointed out that the properties of the interstellar matter (ISM) toward Cyg OB2 12 are not special, while Gredel et al. (2001) suggested that the significant X-ray luminosity of Cyg OB2 12 may affect the ISM in its vicinity.

Nebulae are commonly observed around LBV and post-LBV stars as well as WR stars (e.g., Toalá et al. 2015; Steinke et al. 2016). Kobulnicky et al. (2012) have considered infrared (IR) and millimeter (mm) emission from the Cyg OB2 region, but they do not report on a circumstellar nebular around Cyg OB2 12. To further search for circumstellar matter around Cyg OB2 12, we scrutinized archival data obtained by the *Spitzer* infrared telescope; however, no circumstellar nebula heated by the intense radiation of Cyg OB2 12 is evident (see Figure 1).

2.1. Stellar and Wind Parameters

Clark et al. (2012) provided a comprehensive study of Cyg OB2 12. Stellar and wind parameters were derived from the analysis of optical spectra by means of a non-LTE stellar atmosphere model. For the wind velocity, a typical β-law was used, with $v(r) = v_\infty (1 - b/r)^\beta$, where $b \sim 1$ is a parameter that ensures a smooth connection between the β-law regime and the hydrostatic layer. For the terminal wind velocity, Clark et al. (2012) adopted $v_\infty = 400$ km s^{-1}, while noting that any
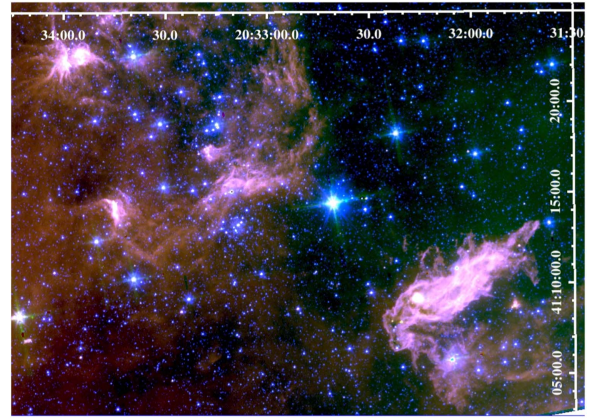

Figure 1. Color composite Spitzer IRAC image (blue: 3.6 μm, green: 4.5 μm, red: 8.0 μm) with Cyg OB2 12 (bright star close to the center. The image size is $24'.1 \times 27'.1$. North is up and east is left.

values between 300 and 1000 km s^{-1} could not be strictly ruled out. Similarly, it was noticed that while values of β below 2 or above 4.5 could not be excluded, the best line fits were obtained for $\beta = 3$.

For modeling the atmosphere and wind of Cyg OB2 12, we made use of the non-LTE stellar atmosphere code PoWR (e.g., Hamann & Koesterke 1998; Hamann & Gräfener 2004; Todt et al. 2015). The PoWR code solves the non-LTE radiative transfer in a spherically expanding atmosphere simultaneously with the statistical equilibrium equations and accounts at the same time for energy conservation. Complex model atoms with hundreds of levels and thousands of transitions are taken into account. Iron and iron-group elements with millions of lines are included through the concept of super-levels (Gräfener et al. 2002). An X-ray field with the observed intensity is artificially added to account for its ionizing effect (Baum et al. 1992). Radiation pressure is consistently included in the treatment of the photosphere, hence providing a realistic description of the photosphere-wind transition region (Sander et al. 2015).

With the parameters and abundances (enhanced nitrogen, depleted carbon and oxygen) adopted from Clark et al. (2012), the synthetic spectrum obtained with PoWR compares well with the observed optical spectrum of Cyg OB2 12 published by the same authors and by Maíz Apellániz et al. (2016), thus confirming their analysis. Our model Hα line is also in good agreement with the observation shown in Figure 1 of Clark et al. (2012).[4] Our fit of Hα and the other Balmer lines required a clumping factor $D = 6$ in the wind. Clark et al. (2012) mention that they applied a clumping value (defined as the inverse of our clumping factor D) of 0.04 at final velocity, but with a radial onset of clumping at 200 km s^{-1}. This seems to result in a similar degree of clumping as our model in those regions where Balmer emissions form. One must keep in mind that there is a degeneracy between clumping factor (at relevant layers) and mass-loss rate when fitting recombination-fed emission lines (Hamann & Koesterke 1998).

In a recent work, Whittet (2015) reassessed the interstellar environments and dust properties toward Cyg OB2 12 and obtained $R_V = 3.05 \pm 0.1$ and $E_{B-V} = 3.33$ mag. Comparing the photometric measurements with the spectral energy

---

[4] Monitoring observations show significant Hα variability (Chentsov et al. 2013, see Section 2.2).
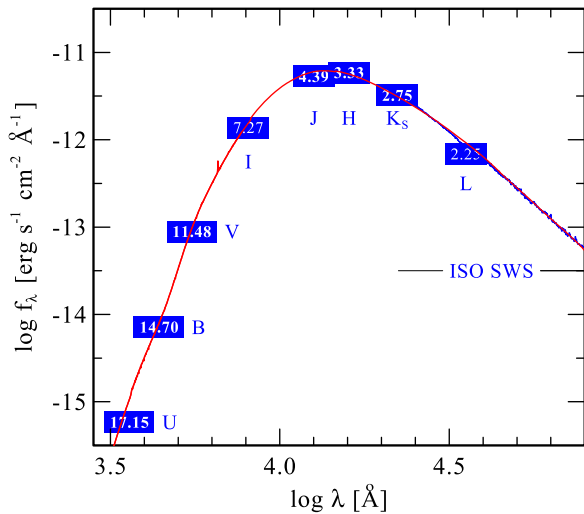
Figure 2. Spectral energy distribution (SED) for Cyg OB2 12; photometric measurements in *UBV* and JHK bands are represented by blue boxes with the magnitudes imprinted. The synthetic SED from a PoWR model with parameters from Table 1 is shown as a red solid line.

distribution from the model (see Figure 2), we obtained good agreement when adopting these values.[5]

Our slightly lower reddening leads to a bolometric luminosity of $\log L_{\rm bol}/L_\odot = 6.22$ compared to 6.28 by Clark et al. (2012). The set of fundamental parameters that we adopt in the following is compiled in Table 1.

With the help of the PoWR model we investigated whether the wind of Cyg OB2 12 can be radiatively driven. The PoWR models compute the work ratio Q defined as the mechanical work per unit time done by the radiation field as compared to the mechanical luminosity of the wind

$$Q \equiv \frac{\int_r \left[g_{\rm rad}(r) - \frac{1}{\rho(r)} \frac{dP_{\rm g}}{dr} \right] dr}{\int_r \left[v \frac{dv}{dr} + \frac{GM_*}{r^2} \right] dr}, \qquad (1)$$

where $g_{\rm rad}$ is the radiative acceleration, $P_{\rm g}$ is the gas pressure, and other symbols have their usual meanings. A hydrodynamically consistent model must give $Q = 1$. When $Q > 1$ the model predicts that the radiation pressure should actually drive a stronger wind (i.e., with higher $\dot{M}$ and/or v_∞). Correspondingly, when $Q < 1$ the model indicates that the radiative acceleration is not sufficient for driving a wind with the adopted parameters.

Using the model parameters from Table 1, we computed this work ratio and obtained $Q \approx 1$, implying that the stellar wind of Cyg OB2 12 is consistent with being radiatively driven. As a test, we also computed models with $v_\infty = 1000\,{\rm km\,s^{-1}}$. The effect of a higher terminal speed for the lines in the optical part of the spectrum is marginal; however, the work ratio Q becomes significantly smaller than unity, implying that such a high wind velocity could not be maintained by radiative driving.

Hence we adopt $v_\infty = 400\,{\rm km\,s^{-1}}$ as most consistent. Taking this as an upper limit for possible velocity

---

[5] Clark et al. (2012) used $E_{\rm B-V} = 3.84$ mag with a reddening parameter $R_{\rm V} = 2.65$.

discontinuities, the strong-shock condition yields 6 MK for the maximum temperature a shock could produce.

The main goal of the present study is to analyze the X-ray spectrum of Cyg OB2 12. For this task, detailed knowledge of stellar wind opacities and the radiation field is required. To compute these quantities, we employed the PoWR code to compute the "cool" wind opacity. This is sufficient because, since no signatures of absorption in the "hot" X-ray emitting plasma are seen in X-ray spectra, the hot plasma component is thus optically thin. Figure 3 shows the radius in the wind where the optical depth for X-rays becomes unity. For the X-rays at wavelengths longward of ≈ 8 Å, the wind is optically thick below $\approx 2\,R_*$. Therefore, if X-ray emission were produced below this radius, one would expect severe wind absorption (Cassinelli et al. 1981; Ignace et al. 2000).

2.2. Spectral and Photometric Variability at Optical and Radio Wavelengths

Cyg OB2 12 is a well-known variable. Gottlieb & Liller (1978) noticed an irregular variability with $\Delta B \approx 0.3$ mag. Among other targets, Laur et al. (2012) also observed Cyg OB2 12 for 300 days in 2011 and confirmed its irregular variability. No clear period was detected, but a timescale for variability of the order of 30 days was established. They found a mild trend in the observed $V - I$ color, and suggested that this could be a manifestation of spectral-type variability. Morford et al. (2016) reported Cyg OB2 12 variability at radio wavelengths.

Salas et al. (2015) conducted a 1.5-year-long photometric study of variability of stars in the Cygnus OB2 association. They concluded that Cyg OB2 12 is an irregular or long-period variable with a period of 54 days, which is a factor of 10 longer than our estimate of the wind flow time. The light curve of Cyg OB2 12 in the *I*-band exhibits changes with an amplitude of $\Delta I = 0.18$ mag.

Besides photometric variability, Cyg OB2 12 also shows spectral variability. Souza & Lutz (1980) found evidence for spectral and radial-velocity changes. In particular, the Hα line centroid moves by more than $30\,{\rm km\,s^{-1}}$. Klochkova & Chentsov (2004) and Chentsov et al. (2013) presented a time series of high-resolution spectra of Cyg OB2 12. They found spectroscopic manifestations of an unstable stellar wind, namely line profile asymmetries and variations that differ from line to line. They suggested that the Hα line profile indicates that some fraction of the wind falls back onto the star.

Clark et al. (2012) gave a detailed review of Cyg OB2 12's variability, and concluded that there is no significant evidence for a long-term evolution of the spectral type over the past 50 years. Short-term variability as observed in Cyg OB2 12 is commonly seen in other luminous blue hypergiants and supergiants as well.

Scuderi et al. (1998) measured the radio spectrum of Cyg OB2 12 and concluded that it is fully consistent with being thermal. Recently, Morford et al. (2016) obtained the first ever resolved detection of Cyg OB2 12 at 21 cm and measured an unclumped mass-loss rate $\dot{M} \approx 5.4 \times 10^{-6}$. Furthermore, they observed a 50 % increase in the mass-loss rate over the 14 d period and discussed previous detections of radio flux variability.

Table 1
Fundamental Parameters of Cyg OB2 12 (Spectral Type B3–4 Ia$^+$)

T_*[a] (kK)	R_*[a] ($R_\odot$)	M_*[a] ($M_\odot$)	$\log \dot{M}$[a] ($M_\odot$ yr^{-1})	v_∞[a] (km s^{-1})	d (kpc)	E_{B-V}[b] (mag)	$\log L_{bol}$[b] ($L_\odot$)	M_V[b] (mag)	Γ_{Edd}	$\log L_x$ (erg s^{-1})
13.7	229	110	−5.52	400	1.75	3.33	6.22	−9.82	0.38	33.8

Notes.
[a] Stellar and wind parameters adopted from Clark et al. (2012).
[b] E_{B-V} taken from the paper by Whittet (2015), which led in consequence to a slight revision of L_{bol} and M_V (see text). L_x refers to the 0.2–10.0 keV band.
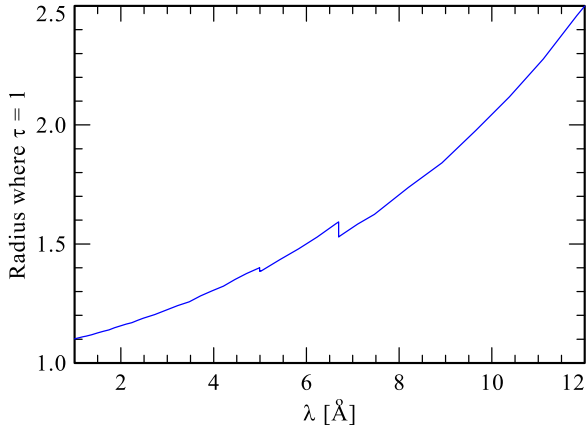

Figure 3. Radius (in units of R_*) where the continuum optical depth reaches unity, as a function of wavelength in the X-ray range, calculated from the PoWR model for the "cool" wind component of Cyg OB2 12 with the parameters from Table 1.

2.3. Binarity Status

The multiplicity of Cyg OB2 12 was carefully investigated by many authors as a possible explanation for its outstanding luminosity and variability. From the analysis of spectroscopic time series, Klochkova & Chentsov (2004) and Chentsov et al. (2013) excluded Cyg OB2 12 as a double-lined spectroscopic binary, but they could not principally rule out a possible binarity.

Caballero-Nieves et al. (2014) conducted a high angular resolution survey of massive OB stars in the Cygnus OB2 association using the fine guidance sensor of the *Hubble Space Telescope (HST)*. A highlight of this study was the discovery of a companion to Cyg OB2 12 with a separation of 63.6 mas. Under the assumption that the projected separation corresponds to the apastron separation, and for a total system mass of $120\,M_\odot$, the orbital period would be ≈ 30 years and the orbital separation $\approx 104\,R_*$ or ≈ 110 au. The secondary is $\Delta V \approx 2.3$ fainter than the primary.

Maryeva et al. (2016) used speckle interferometry and confirmed the detection of a second component in Cyg OB2 12. They were able to measure the changes in the position angle of the secondary component, and suggested that the binary period is ~100 years. They discovered an even fainter third component in the Cyg OB2 12 system.

The brightness ratio ($\Delta V \approx 2.3$) suggests that the secondary, most likely also a hot star, must have a much smaller radius (e.g., like an OB star of lower luminosity class). The wind of such a putative companion is expected to be quite fast. For the purpose of an estimate, we might imagine an O9.5 II star with parameters as recently derived for δ Ori: $\log L_{bol}/L_\odot \approx 4.8$, $\dot{M} \approx 2 \times 10^{-7}\,M_\odot$ yr^{-1}, and $v_\infty \approx 2000$ km s^{-1} (Shenar et al. 2015). When such a fast wind collides with the denser and slower wind of a B hypergiant, strong X-ray emission and high shock temperatures should result (e.g., Stevens et al. 1992).

3. *Chandra* Observations of Cyg OB2 12

In this paper we report X-ray observations[6] of Cyg OB2 12 obtained on 2015 January 14 with an exposure time of 138 ks using the *Chandra* HETG spectrometer (Canizares et al. 2005). The HETGS spectra cover a wavelength range from about 1 to 30 Å, as dispersed by two types of grating facets, the High Energy Grating (HEG) and the Medium Energy Grating (MEG), with resolving powers ranging from 100 to 1000, and an approximately constant FWHM of 0.012 Å for HEG and 0.023 Å for MEG.

The *Chandra* data were reprocessed with standard *Chandra* Interactive Analysis of Observations (CIAO) programs (Fruscione et al. 2006) to apply the most recent calibration data (CIAO version 4.6 and calibration database version 4.6.5). The data are thus composed of four orders per source per observation: the positive and negative first orders for each grating (MEG and HEG), which have different efficiencies and resolving powers. The default binning over-samples the instrumental resolution by about a factor of four. The merged HETGS flux spectrum is shown in Figure 4.

When operating together with HETGS, the ACIS-S also simultaneously obtains a zeroth-order, low-resolution X-ray spectrum that can be a useful complement to the high-resolution spectrum, especially in the vicinity of Fe K, though care must be taken to assess photon event pileup. Figure 5 shows the zeroth-order spectrum of Cyg OB2 12.

We modeled the spectrum primarily using the Interactive Spectral Interpretation System (Houck & Denicola 2000), which implements interfaces to the AtomDB (Foster et al. 2012) and to XSPEC models (Arnaud 1996). We fit a three-temperature apec model to the high-resolution and zeroth-order spectrum. We allowed relative abundances of prominent species (Mg, Si, S, Fe) to float since this gave a somewhat better fit. Formally, the best fit to the X-ray spectrum (as shown in the figures of this paper) was obtained with slightly sub-solar abundances (factors compared to solar: 0.6 for Mg, 0.7 for Si, 0.9 for S, and 0.8 for Fe). This could be in part due to degeneracies between discrete temperature components, abundances, and absorption (both line-of-sight and wind-intrinsic), and not be considered to be real.

Since the absorption is large, $N_H \sim 10^{22}$ cm^{-2}, the lowest-temperature component in the tree-temperature model, is poorly constrained. Using a two-temperature model we obtain a fit of similar quality with a slightly lower absorption and lower temperature for the middle component. This illustrates some of the degeneracy in global modeling. Either fit can serve

---

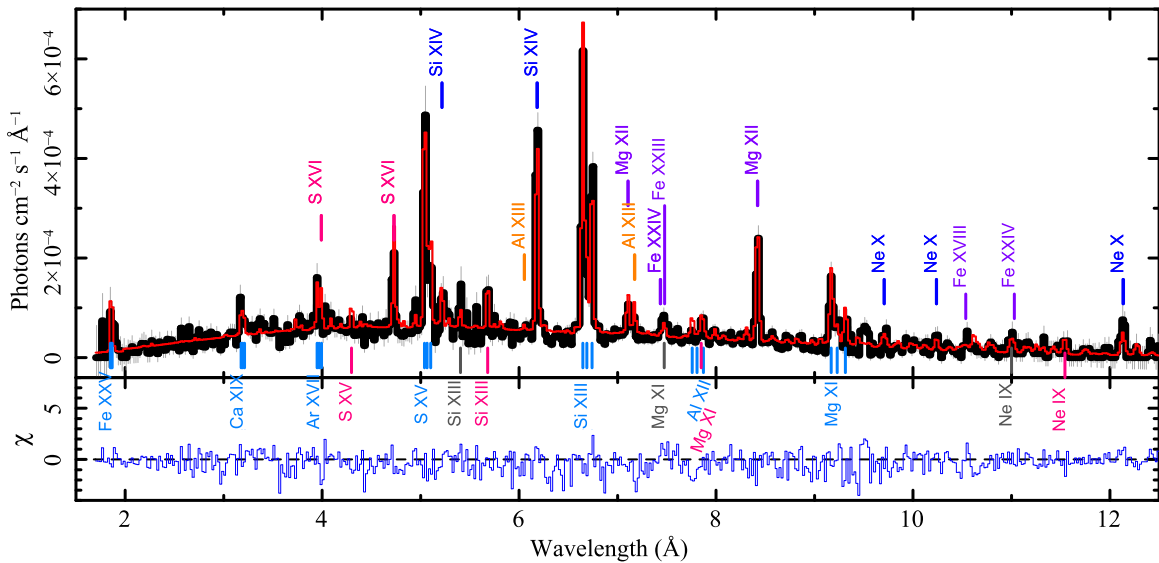[6] *Chandra* Observation Identifier 16659.

Figure 4. *Chandra* HETGS spectrum of Cyg OB2 12 with prominent lines identified. Lines from He-like ions are marked below the spectrum, while H-like and other Fe lines are marked above the spectrum. The observation is in black, with a model in red, and residuals in the lower panel in blue. For illustration only, counts were converted to photon flux using the instrument responses (but still include the instrumental resolution), combining the positive and negative first orders of the spectrum from the HEG and MEG arms.
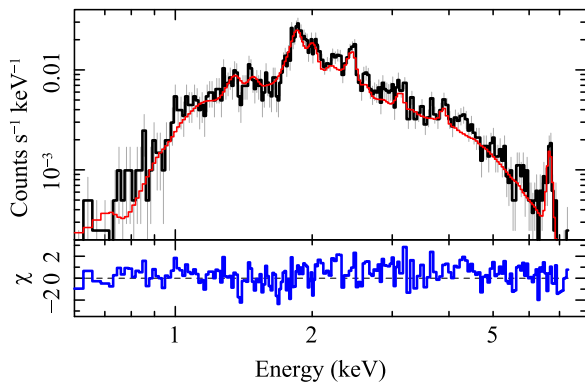

Figure 5. HETGS zeroth-order count spectrum (black histogram with gray error bars), plasma model (red), and residuals (lower panel, blue).

Table 2
Parameters from Simultaneous Fits of the MEG, HEG, and Zeroth-order Spectra of Cyg OB2 12 in the 0.6–7.0 keV Range with Three-temperature or Two-temperature apec Plasma Models Accounting for Interstellar Absorption (via phabs) (Balucinska-Church & McCammon 1992; Smith et al. 2001)

	Three-temp.	Two-temp.
N_H [10^{22} cm^{-2}]	2.05 ± 0.05[a]	1.8 ± 0.03
kT_1 [keV]	0.20 ± 0.04	...
kT_2 [keV]	0.81 ± 0.1	0.77 ± 0.1
kT_3 [keV]	1.86 ± 0.2	1.95 ± 0.2
EM_1 [10^{56} cm^{-3}]	33.89 ± 13.60	...
EM_2 [10^{56} cm^{-3}]	2.50 ± 0.34	2.60 ± 0.34
EM_3 [10^{56} cm^{-3}]	1.01 ± 0.30	1.10 ± 0.30
f_x [10^{-12} erg cm^{-2} s^{-1}]	1.9 ± 0.2[b]	

Notes.
[a] Error margins refer to 1σ uncertainty.
[b] Observed flux in the 0.6–7.0 keV band.

as an equally good basis for detailed line measurement by providing a continuum model and approximate temperatures. We list the model parameters in Table 2. The models are in good agreement with those previously published based on the analysis of low-spectral resolution *XMM-Newton* spectra. The absorbing column derived from spectral fitting corresponds well with the interstellar reddening, using the conversion factor $N_H \approx E_{B-V} \times 5.8 \, 10^{21}$ cm^{-2} (Bohlin et al. 1978).

The observed flux in the 0.2–10 keV band is $f_x \approx 1.9 \times 10^{-12}$ erg cm^{-2} s^{-1}. Using the column density from the two-temperature fit, the (unabsorbed) model luminosity becomes $L_x \approx 6.8 \times 10^{33}$ erg s^{-1}, or $\log L_x/L_{bol} \approx -5.7$, which is a factor of two larger than that found in previous studies (e.g., Rauw 2011).

With the caveat that the contribution of the soft plasma components might be underestimated, the emission-measure-weighted temperature of the X-ray emitting plasma is ≈ 13 MK (1.1 keV), while the hottest plasma component has a temperature of ≈ 22 MK (1.9 keV). This is significantly higher than could be explained by intrinsic shocks in the relatively slow

wind of Cyg OB2 12. The high temperature could be explained, however, by a collision of a fast wind with $v \sim 1000$ km s^{-1} from a presumable OB-type companion with the slow wind of the blue hypergiant. The simple colliding wind model (see Equations (1)–(4) in Luehrs 1997) allows us to crudely estimate the possible location of the wind–wind collision region in Cyg OB2 12. The colliding wind zone is expected to be concave around the O-type component, with the apex of the colliding wind cone located at about ≈ 40 au from the secondary ($\approx 1000 \, R_{*,O}$ assuming $R_{*,O} = 9 \, R_\odot$) and ≈ 70 au ($\approx 66 \, R_{*,BI^+}$) from the primary. This is a prediction that, in principle, could be checked by investigating the high-resolution X-ray spectra (see Section 3.2.1).

In such a wide binary the plasma cooling in the colliding wind zone is adiabatic. The resulting X-ray luminosity scales inversely with the binary separation (Stevens et al. 1992). Therefore, for a binary on elliptic orbit, the modulation of X-ray flux on the timescale associated with the binary period is
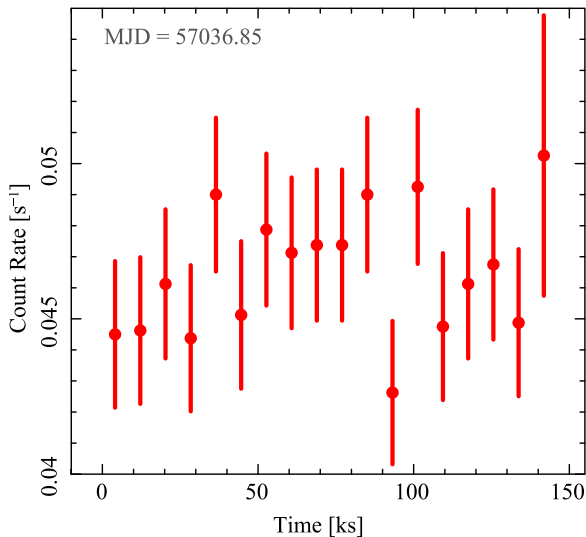
Figure 6. *Chandra* HETG X-ray light curve of Cyg OB2 12 in the 0.6–7.0 keV band during our observation on 2015 Jan 14. The data are binned to 8 ks. Error bars indicate 1σ statistics.

Figure 7. X-ray flux of Cyg OB2 12 in the 0.5–10 keV band as measured at different epochs within ∼10 years. All data points except the first and the last ones show X-ray fluxes from *XMM-Newton* observations, adopted from Cazorla et al. (2014). The first red point is from a serendipitous *Chandra* observation, while the last red point represents our *Chandra* observation on 2015 Jan 14 (MJD 57036). The error bars are smaller than the size of the symbols. The inset shows that significant X-ray variability is also observed on a shorter timescale (≈30 days).

expected. In the case of Cyg OB2 12, one would expect to observe X-ray variability on timescales >30 years. This prediction can also be checked observationally.

3.1. Temporal Variations of the X-Ray Flux

The X-ray light curve during our *Chandra* HETG observation (36 hr exposure time) is shown in Figure 6. It is consistent with being constant, albeit the variance seems to increase toward the end of the observation. Compared to the exposure time, the characteristic wind flow time in Cyg OB2 12 is long, $t_{\rm flow} = R_* v_\infty^{-1} \approx 120$ hr or 5 days. Any variability on a much shorter timescale thus would be difficult to explain.

Cyg OB2 12 has been sporadically observed in X-rays since this range became accessible (Harnden et al. 1979; Kitamoto & Mukai 1996). Waldron et al. (1998) pointed out that in the 1980s and 1990s, the X-ray emission of Cyg OB2 12 may have been steadily increasing at a slow rate. They also reported short-term variability at the level of 20%, but were not able to firmly attribute this variability to the star itself (due to suspected instrumental effects).

Albacete Colombo et al. (2007) reported a roughly linear decrease of the *Chandra* ACIS count rate of Cyg OB2 12 from ≈ 0.18 count s^{-1} to ≈ 0.16 count s^{-1} during a 98 ks exposure.

Rauw (2011) analyzed six *XMM-Newton* observations of the Cyg OB2 region (four in 2004 and two in 2007) with a total exposure time of 148 ks. Cyg OB2 12 revealed variability at a 10% level, with timescales from a few days to a few weeks. A larger variation of the X-ray flux (40%) was seen between observations made in 2004 and 2007. These variations were attributed to changes in the column density of absorption, while the plasma temperature was found to be relatively constant. The Cyg OB2 12 X-ray spectra were best fitted by multi-temperature plasma models with $kT_1 = 0.76 \pm 0.03$ and $kT_2 = 2.03 \pm 0.19$ keV.

Further investigating the temporal evolution of the X-ray flux from Cyg OB2 12, Cazorla et al. (2014) also included observations obtained by the *Swift* and *Suzaku* X-ray telescopes. A decrease of X-ray flux between 2004 and 2011
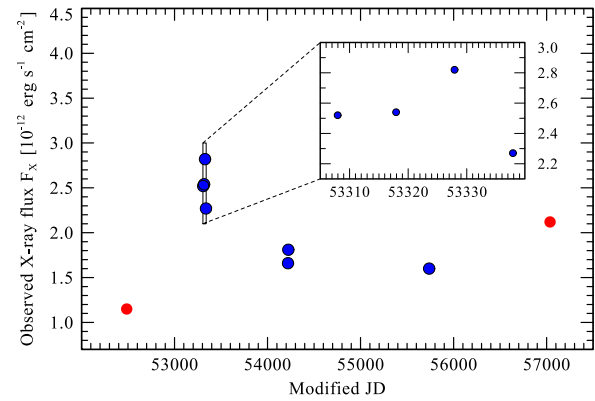
(MJD 53000–56000) by 40% earlier noticed by Rauw (2011) was confirmed.

Our latest observation yields a flux that is 33% higher than the previous *XMM-Newton* observation obtained on 2011-06-25 (MJD 55737), thus showing an opposite trend than before.

We have additionally derived the flux from the earliest, serendipitous *Chandra* HETG observation (Observation Identifier 2572, observed in 2002); while far off-axis and not useful for high-resolution analysis, that observation is sufficient to determine a flux of 1×10^{-12} erg cm^{-2} s^{-1} from the nearly 1000 counts in the two dispersed spectra on the detector array. Other previous *Chandra* observations of Cyg OB2 12 without grating were affected by pileup (Rauw et al. 2015) and are therefore not useful for flux estimates.

Figure 7 shows the evolution of the X-ray flux from Cyg OB2 12 over time, combining our recent observation with all useful previous data from *Chandra,* as well as that from *XMM-Newton.*[7] The X-ray flux varied by up to a factor of two.

If the X-rays from Cyg OB2 12 were powered by wind–wind collision in a binary, modulations on the orbital timescale would be expected, especially if the orbit was eccentric. The recent discovery of a binary companion with a $\gtrsim$30-yr period (cf. Section 2.3) supports this expectation. However, Figure 7 does not clearly suggest such a regular behavior. On the contrary, short-term variability has been observed too (see insert in Figure 7). As made clear from the first four *XMM-Newton* observations, the X-ray flux can change by ∼20% within just one month (Rauw 2011). Hence, one cannot exclude that the observed light curve reflects only random variability.

3.2. Analysis of the X-Ray Emission Line Spectrum

3.2.1. Lines of He-like Ions

The HETGS spectrum of Cyg OB2 12 is dominated by strong emission lines (see Figure 4). Among them are the

---

[7] The two instruments are cross-calibrated within ∼10%; see http://xmm2.esac.esa.int/external/xmm_sw_cal/calib/documentation/index.shtml.
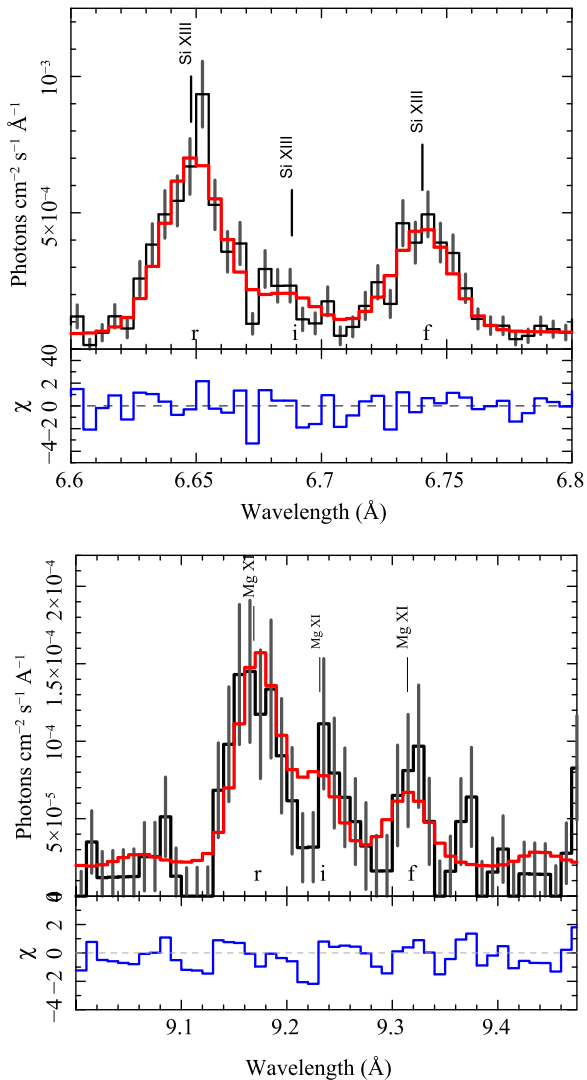
Figure 8. Si XIII (top) and Mg XI (bottom) fir triplets in the MEG first-order spectra of Cyg OB2 12. In each plot, the top panels show the photon count spectra as a black histogram, with the best-fit model as the red histogram. The rest-frame wavelengths for the resonance, intercombination, and forbidden lines are marked. Residuals are shown in the lower part of each panel.

prominent lines of the He-like ions Si XIII and Mg XI (Figure 8). These ions show characteristic "fir triplets" of a forbidden (z), an intercombination ($x + y$), and a resonance (w) line (Gabriel & Jordan 1969).

In order to measure the f/i ratios from this spectrum, $\mathcal{R}(r)$, as accurately as possible, we used the global multi-temperature fit to first provide an approximate plasma model. Then, we fitted the lines locally using the density-dependent emissivities for Mg or Si.[8] The fits are shown in Figure 8, and the obtained values for $\mathcal{R}_{obs}$ are given in Table 3 together with their 90% confidence intervals.

Considering the theory, the ratio of fluxes between the forbidden and intercombination lines, $\mathcal{R}(n_e, T_{rad}) = z/(x + y)$, is sensitive to the UV radiative field and to the electron density (e.g., Porquet et al. 2001). Strong UV radiation leads to a significant depopulation of the upper level of the forbidden line

---

[8] See http://space.mit.edu/cxc/analysis/he_modifier for details, emissivity data, and code.

Table 3
Ratios $\mathcal{R} = f/i$ for He-like ions in the HETGS Spectrum of Cyg OB2 12

Ion	$\lambda(w)$ [Å]	$\mathcal{R}_{obs}$	R_0
Si XIII	6.65	3.22 (2.5 … 3.9)	3.02
Mg XI	9.17	0.78 (0.2 … 2.3)	3.70

Notes. Wavelengths refer to the resonance lines (w component). For $\mathcal{R}_{obs}$, the measured values are given together with their 90% confidence intervals. The last column gives the asymptotic ratio R_0 that has been adopted for the calculation (see the text).

to the upper levels of the intercombination lines (Blumenthal et al. 1972). For the characteristic densities of OB and WR star winds, this is the dominant mechanism for forbidden line depopulation (e.g., Leutenegger et al. 2007; Waldron & Cassinelli 2007; Oskinova et al. 2012). Since the radiation field dilutes with distance from the stellar surface, the ratio between forbidden and intercombination lines provides information about the location of the X-ray emitting plasma.

The upper level of the forbidden line transition can also be depopulated by electron collisions. However, to be significant this process requires electron densities that are comparable to the "critical" value n_c, which is 4×10^{13} cm^{-3} and 6×10^{12} cm^{-3} for Si XIII and Mg XI, respectively (Blumenthal et al. 1972).

Cyg OB2 12 has relatively dense wind, low effective temperature, and yet a very hot X-ray plasma. For these conditions, it is not clear a priori which mechanism of forbidden line depopulation dominates. Hence, in order to correctly apply the fir diagnostic, we employed our PoWR model (cf. Section 2.1). For modeling the f/i ratio, we follow the recipe by Shenar et al. (2015), which is based on Blumenthal et al. (1972).

For the wavelengths of the depopulating transitions (865 Å for Si XIII, 1034 Å for Mg XI) we extract the mean intensities at each radial layer in the stellar wind, as provided by our PoWR model calculation for Cyg OB2 12. Note that all effects, such as diffuse emission, limb darkening, and attenuation of UV flux in the wind, are automatically included in the model in a consistent manner. The density in the wind is also taken from our PoWR model. Taking the same density for the collisional depopulation relies on the assumption that the densities in the shock-heated plasma are similar to the smooth-wind densities at the same radii. This is a reasonable first approximation, since hydrodynamical simulations for wind-embedded shocks powered by the line-driving instability did not predict large overdensities in the shocked material (Feldmeier et al. 1997).

Furthermore, the modeling of the f/i ratio requires the relevant atomic data. The transition wavelengths and oscillator strengths are extracted from the NIST database. The asymptotic value for the f/i ratio, R_0, which enters the the theoretical computation of $\mathcal{R}(r)$, is slightly temperature-dependent; the values adopted here are read off from Figure 8 in Porquet & Dubau (2000) for the highest temperatures provided.

The results of our f/i analysis are illustrated in Figure 9. For the He-like ions Si XIII and Mg XI, the predicted f/i ratio $\mathcal{R}(r)$ is plotted as a function of the radial location r of the emitting plasma.

Different temperature plasma components (with 6 MK and 20 MK) may contribute significantly to the emission in Mg XI and Mg XII lines. A better measurement of the S XV, Si XIII, and
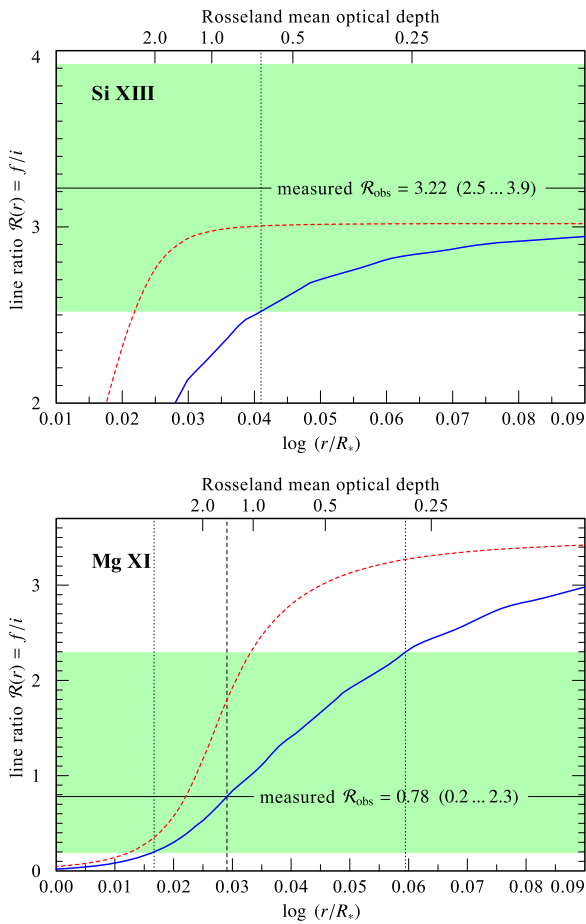
Figure 9. Theoretical $\mathcal{R}(r) = f/i$ as a function of the radial location of the X-ray emitting plasma for the fir triplet from Si XIII (top panel) and Mg XI (bottom). The red dashed curves are computed assuming that the depopulation of the forbidden level is by the photoexcitation only, while the blue solid curves include the contributions of collisions. In each panel, the measured value is indicated by a horizontal black line, while the green-shaded band indicated its error margin. The intersections of $\mathcal{R}(r)$ (blue curve) with the observed values $\mathcal{R}_{obs}$ and their error margins are indicated by vertical dashed and dotted lines, respectively.

Mg XI line ratios would help to constrain the relative contributions of plasma components to the line spectrum.[9]

First, we test whether collisional or radiative excitation is the dominant process for the forbidden line depopulation. The calculations reveal that in the *wind* of Cyg OB2 12, neither the UV field (which is weak due to the low effective temperature of the star) nor the electron collisions are able to depopulate the forbidden line upper state! With growing distance r, the predicted *f/i* ratio $\mathcal{R}(r)$ soon approaches the limiting value R_0. Note that Figure 9 zooms-in at the photosphere/wind transition region, as can be recognized from the Rosseland-mean optical depth scale indicated at the top of the diagrams.[10] The red dotted line is calculated for zero electron density, i.e., neglecting collisional depopulation, while the blue curves take collisional depopulation into account. The large difference between these two curves reveals the leading role of collisions for this process in these layers.

---

[9] These arguments were suggested by the reviewer.
[10] The stellar radius R_* refers, by our definition, to $\tau_{\mathrm{Rosseland}} = 20$, while $\tau_{\mathrm{Rosseland}} = 2/3$ is the radius from which most of the photospheric flux escapes.

The (blue) theoretical curve may now be compared to the measured *f/i* ratio $\mathcal{R}_{obs}$, which is also indicated in each of the panels of Figure 9 by a horizontal line together with the uncertainty of the measurements (90% confidence interval, green-shaded band).

For Si XIII the measured $\mathcal{R}_{obs}$ is consistent with the limiting R_0, i.e., with the absence of any depopulating process. Hence, the X-ray emitting plasma could reside anywhere in the wind, and its location cannot be constrained.

A better constraint is provided by Mg XI. As can be seen from the lower panel of Figure 9, the observed ratio of forbidden to intercombination lines indicates that, at least within the 90% confidence interval, the measured $\mathcal{R}_{obs}$ is *not* consistent with R_0, i.e., depopulation is required. Densities that are comparable to n_c are only encountered in or very close to the photosphere. Hence we must conclude from Figure 9 that the fir triplet of Mg XI is emitted from plasma located at $r < 1.15\,R_*$, i.e., practically directly at the photosphere. In this case, the X-ray emission lines shall be narrow and would be unresolved even with HETGS grating spectrometry. This is because the wind expansion velocity at these radii is very small. Moreover, as can be seen in Figure 3, below $1.8\,R_*$, the stellar wind of Cyg OB2 12 is optically thick for radiation at λ 9.2 Å. Therefore, if radiation could originate in deeper wind layers, the spectral signatures of stellar wind absorption could be expected. With all these in mind, the investigation of spectral lines should further help in constraining the hot plasma location.

3.2.2. X-Ray Emission Line Profiles

X-ray line profiles formed in a stellar wind are influenced by two effects, the Doppler shift due to the wind expansion, and the absorption that is caused by the continuum opacity of the cool wind material. The Doppler shifts can broaden the emission line profile up to $\pm v_\infty$ (Macfarlane et al. 1991; Ignace 2001; Owocki & Cohen 2001), while absorption and obscuration affect the back hemisphere more than the front hemisphere and thus cause the line profiles to become skewed and effectively blueshifted (Oskinova et al. 2006). Especially if X-rays were produced close to the photosphere, we would expect to find these signatures of wind absorption. As can be seen from Figure 3, at $1.18\,R_*$ the optical depth for X-rays already exceeds unity for any wavelengths >3 Å and increases further with wavelength. At least such lines as Mg XII $\lambda 8.42$ Å and Mg XII $\lambda 9.17$ Å should show signs of wind absorption.

To model the X-ray emission line profiles for Cyg OB2 12, we perform the same kind of calculations as described in Oskinova et al. (2006). The wind density and the opacities are again taken from our PoWR model for this star. The main parameter of these calculations is the radius at which the X-ray plasma appears; since the emissivity scales with the square of the density, most of the photons are produced close to this onset radius.

Based on the result from the fir analysis (Section 3.2.1), we adopt an onset radius for X-ray emission close to the photosphere (its precise value is not relevant). The model then predicts that the profiles would not be broadened by the wind velocity, because the latter is still tiny close to the photosphere. The FWHM of the line profile would be only $\approx 20\,\mathrm{km\,s^{-1}}$, i.e., the observed profile should only reflect the instrumental profile, which is much broader.

Figure 11. Bold ovals show the 1σ confidence contours for the Doppler shift of the centroid (*x*-axis) and the width (FWHM, *y*-axis) for the Si XIV (red) and the Mg XII (blue) lines, respectively. Gray contours refer to 90% confidence.
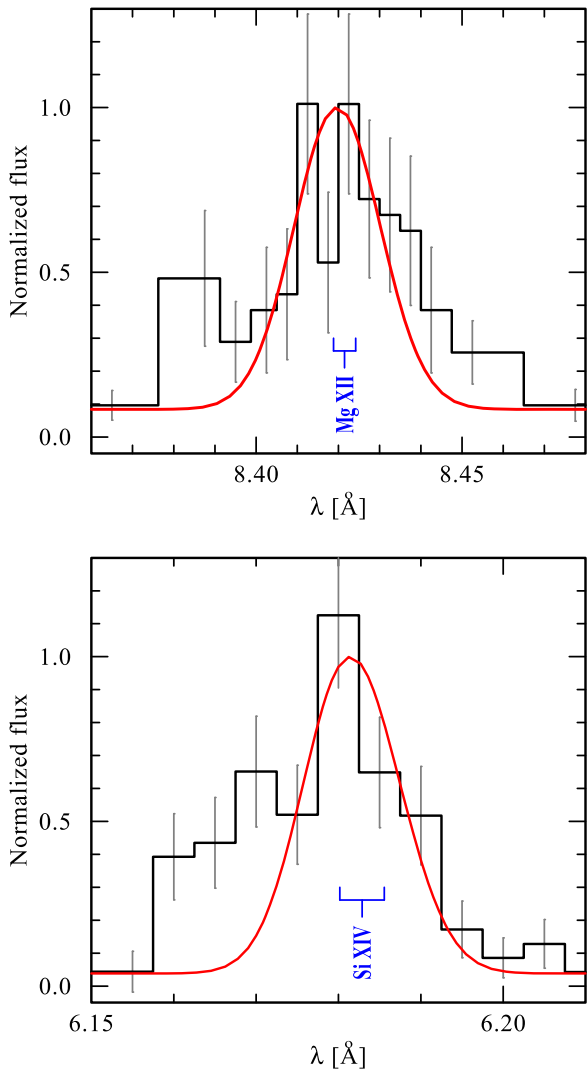
Figure 10. Lines of Mg XII (top panel) and Si XIV (bottom) in the (co-added MEG±1) spectrum of Cyg OB2 12 (black histograms); the red curves show a model profile assuming that the X-ray-emitting plasma expands according to a β-velocity law with $v_\infty = 400$ km s^{-1}. The rest-frame wavelengths of the doublet components are indicated in blue.

This expectation can be tested with the resonance lines of the hydrogen-like ions Mg XII at 8.42 Å and Si XIV at 6.18 Å. Figure 10 shows that in both cases the observed profile is significantly broader than the predicted profile convolved with the instrumental response. In other words, the *Chandra* HETGS observation resolves these profiles.

To quantify the broadening of these lines, we fit their profiles with apec models over a small region of interest for each line, assuming that all lines in the region have the same Gaussian shape and a common Doppler shift.

The fits and confidence contours obtained with the Interactive Spectral Interpretation System software package are shown in Figure 11. Both lines are intrinsically broadened. For both lines, the best fit indicates FWHM values in excess of 700 km s^{-1}. The lines are hardly Doppler-shifted against their rest wavelengths; centroid shifts by more than 150 km s^{-1} can be ruled out. Such broad and unshifted lines are not expected from the Cyg OB2 12 wind model.
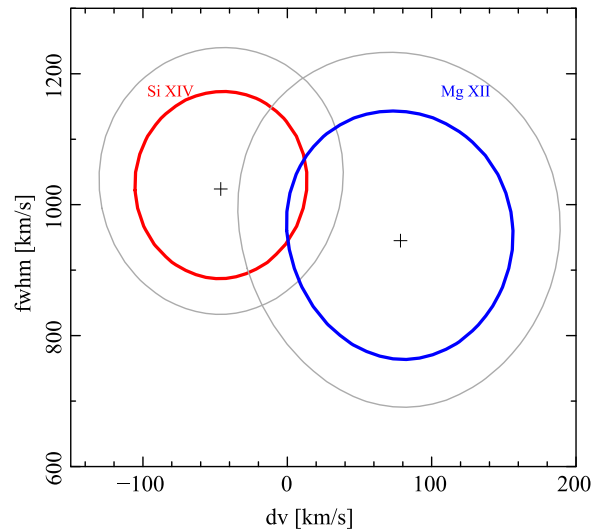
4. Discussion and Summary

4.1. A Scenario for the Origin of X-Ray Emission from Cyg OB2 12.

The analysis of new high-resolution X-ray spectra of Cyg OB2 12, combined with modeling of its stellar wind by a non-LTE stellar atmosphere, provided fresh insights on the nature of Cyg OB2 12. Considering all observational facts together, the X-ray observations of Cyg OB2 12 are best explained by a colliding winds scenario.

(1) The X-ray spectrum from Cyg OB2 12 is well described by a thermal plasma in collisional equilibrium. Because of high interstellar absorption, only the rather hard part of the spectrum is observable. The highest temperature plasma components with $T_X \gtrsim 20$ MK cannot be explained by intrinsic shocks in the relatively slow wind of Cyg OB2 12 ($v_\infty \approx 400$ km s^{-1}).

(2) The X-ray luminosity is higher than expected from a mid-B spectral type.

(3) The X-ray emission lines are broad. The line width (up to 1000 km s^{-1}) indicates that the X-ray emitting plasma moves with higher velocities than possible in the slow, cool wind of Cyg OB2 12 ($v_\infty \approx 400$ km s^{-1}).

(4) The stellar wind opacities computed with our non-LTE models are high. If X-rays were to emerge from the inner wind, we would expect to see strong signs of wind attenuation in X-ray spectra. These are not observed.

(5) The non-LTE stellar atmosphere models indicate that collisions dominate over the UV de-excitation of the forbidden lines in the He-like triplets seen in Cyg OB2 12's X-ray spectrum. Hence the measured forbidden-to-intercombination line-flux ratios provide information about plasma densities. Based on the analysis of Mg XI lines, we conclude that the X-ray plasma has densities in excess of 10^{13} cm^{-3}. Such high densities could be achieved either at Cyg OB2 12's photosphere, or in a hypothetical colliding wind region.

(6) Assuming that the secondary is an O-type star, we estimate that the apex of the colliding wind shock is located at $\sim 1000\,R_*$, O from the secondary (see Section 3). At these distances, the UV flux from the secondary is strongly diluted, and does not dominate the forbidden line depopulation. To fully understand X-ray emission from Cyg OB2 12 we need to better establish its binary properties.

On the basis of the above points, and taking into account the recent detection of a close-by companion to Cyg OB2 12, the colliding wind scenario seems to provide the most plausible explanation. This conclusion requires further quantitative testing that will become possible only when the secondary type and orbital parameters are known. Until then, the question of whether the density required for forbidden line depopulation can indeed be produced in the colliding wind zone of Cyg OB2 12 remains open.

The high-temperature plasma must occur in quite dense regions. For a colliding wind zone, the pre-shock densities of the primary and the secondary winds are several orders of magnitude lower than needed to explain the f/i line ratios. In radiative shock, high densities can be achieved in the post-shock cooling zone, but those regions are deficient in X-ray-emitting gas. Radiative shocks are known to be unstable via thin-shell instability (Vishniac 1994); perhaps some form of dynamical mixing allows for both high densities and high temperatures to coexist.

It is informative to compare the f/i ratios measured in Cyg OB2 12 (see Table 3) with those determined for the well-known colliding wind binaries, e.g., the $f/i \approx 5$ ratio measured in the HETGS spectrum of Mg XI in the WR-binary WR 140 is consistent with the absence of the forbidden line depopulation mechanism (Pollock et al. 2005). Similarly, in case of the LBV-binary η Car, Henley et al. (2008) measured in the HETGS spectrum of Si XIII the ratio $f/i > 5$.

The hydrodynamic simulations of the massive binary η Car display quite hot gas components and high densities (Parkin et al. 2011). η Car involves a primary with a dense and relatively slow wind orbited by a secondary with a considerably faster wind. The models indicate that orbital motion of the stars in η Car helps to stabilize the wind collision zone against thin-shell instabilities. The orbital period for η Car is only ~ 5 years; the longer orbital period of Cyg OB2 12 could allow for stronger thin-shell instabilities and a greater level of mixing, resulting in the presence of hot, dense zones.

4.2. On the Binary Evolutionary History of Blue Hypergiants

The binary hypothesis is further supported by another consideration. Using archival X-ray data, we conducted a survey of all 16 known Galactic blue hypergiants. We found that the majority of these objects were not detected in X-rays. Some of the hypergiants, namely HD 80077, Wd 1-5, Wd 1-13, and HD 160529, were observed with modern telescopes and deep exposures, putting low upper limits on their respective X-ray luminosities. For example, the upper limit for HD 160529 (B8-A9 Ia$^+$) is $\log(L_x/L_{bol}) < -8.5$ (Nazé et al. 2012). Especially interesting are the early-type hypergiants HD 169454 (B1 Ia$^+$) and ζ^1 Sco (B1.5 Ia$^+$), both of which were not detected during the *ROSAT* All-Sky Survey, with an upper limit for ζ^1 Sco at $\log(L_x/L_{bol}) < -8$. It appears safe to conclude that blue hypergiants, in general, are not significant

X-ray sources, with the X-ray luminosity not exceeding $\sim 10^{-9}$ of their bolometric luminosity.

The two blue hypergiants that are outstandingly X-ray bright are BP Cru (B1 Ia$^+$) and the subject of our study, Cyg OB2 12 (B3–4 Ia$^+$). Both of them are binaries. BP Cru is a well-known high-mass X-ray binary where a neutron star accretes the wind of its hypergiant companion (e.g., Kaper et al. 2006). Its X-ray luminosity, $L_x \sim 10^{37}$ erg s^{-1} is determined by the accretion rate onto the neutron star. The X-ray luminosity of Cyg OB2 12, however, is too low to suggest such a scenario. Except these two, no other binary hypergiants are confirmed so far. Though the number of known Galactic hypergiants is small, the very low binary fraction among them is in stark contrast with the general OB star population.

We suggest that all blue hypergiants are the products of binary evolution. Clark et al. (2014) discussed in detail the role of binarity in explaining the apparently single blue hypergiant Wd 1-5. In the case of Cyg OB2 12, the single star evolutionary models do not predict such extreme stars (Ekström et al. 2012). Therefore, we propose that Cyg OB2 12 is either a former mass gainer in a very massive system with a large initial mass ratio, or a merger product.

In the former case if it would have been possible for the system to increase its orbital separation following the mass exchange, then the presently fainter companion of Cyg OB2 12 may be the stripped remnant of the primary, e.g., a helium star of WR-type. Such a star would have a strong and fast stellar wind, and help to explain the observed X-ray emission. However, such a WR companion would have a spectrum dominated by emission lines. We carefully considered the spectrum of Cyg OB2 12 for such contamination, but we do not find any traces of WR features.

It seems more plausible that Cyg OB2 12 is a result of a merger. Blue supergiant stars are expected to be mergers resulting from binary evolution (Podsiadlowski et al. 1992). We are not aware of detailed binary evolution models for blue hypergiants. However, the low binary fraction among these types of stars, along with their enhanced nitrogen abundances (Clark et al. 2012), may be a smoking gun pointing to their origin.

We propose the following scenario. The progenitor of Cyg OB2 12 was initially a hierarchical multiple system, as is common among massive stars (e.g., Shenar et al. 2015). The eccentric Kozai–Lidov mechanism (Naoz & Fabrycky 2014) caused the strong inclination and eccentricity fluctuations, resulting in tidal tightening of the inner binary. This inner tight binary merged and is observed today as the blue hypergiant. The initial tertiary is the present day binary component of Cyg OB2 12. These two stars form a colliding wind system where the slow and dense wind of a blue hypergiant collides with the fast wind of its late O-type companion.

Furthermore, we have shown that the single blue hypergiants are X-ray-dim. If observed, bright X-ray emission from a blue hypergiant is a strong indicator of its binarity. We conclude that the majority of Galactic blue hypergiants are currently single stars but with previous binary evolutionary history.

ORCID iDs

D. P. Huenemoerder ● https://orcid.org/0000-0002-3860-6230
T. Shenar ● https://orcid.org/0000-0003-0642-8107
R. Ignace ● https://orcid.org/0000-0002-7204-5502

References

Albacete Colombo, J. F., Flaccomio, E., Micela, G., Sciortino, S., & Damiani, F. 2007, A&A, 464, 211
Arnaud, K. A. 1996, in ASP Conf. Ser. 101, Astronomical Data Analysis Software and Systems V, ed. G. H. Jacoby & J. Barnes (San Francisco, CA: ASP), 17
Balucinska-Church, M., & McCammon, D. 1992, ApJ, 400, 699
Barniske, A., Oskinova, L. M., & Hamann, W.-R. 2008, A&A, 486, 971
Baum, E., Hamann, W.-R., Koesterke, L., & Wessolowski, U. 1992, A&A, 266, 402
Blumenthal, G. R., Drake, G. W. F., & Tucker, W. H. 1972, ApJ, 172, 205
Bohlin, R. C., Savage, B. D., & Drake, J. F. 1978, ApJ, 224, 132
Caballero-Nieves, S. M., Nelan, E. P., Gies, D. R., et al. 2014, AJ, 147, 40
Canizares, C. R., Davis, J. E., Dewey, D., et al. 2005, PASP, 117, 1144
Cassinelli, J. P., Waldron, W. L., Sanders, W. T., et al. 1981, ApJ, 250, 677
Cazorla, C., Nazé, Y., & Rauw, G. 2014, A&A, 561, A92
Chentsov, E. L., Klochkova, V. G., Panchuk, V. E., Yushkin, M. V., & Nasonov, D. S. 2013, ARep, 57, 527
Chini, R., Hoffmeister, V. H., Nasseri, A., Stahl, O., & Zinnecker, H. 2012, MNRAS, 424, 1925
Clark, J. S., Najarro, F., Negueruela, I., et al. 2012, A&A, 541, A145
Clark, J. S., Ritchie, B. W., Najarro, F., Langer, N., & Negueruela, I. 2014, A&A, 565, A90
Crowther, P. A., Schnurr, O., Hirschi, R., et al. 2010, MNRAS, 408, 731
Ekström, S., Georgy, C., Eggenberger, P., et al. 2012, A&A, 537, A146
Feldmeier, A., Puls, J., & Pauldrach, A. W. A. 1997, A&A, 322, 878
Foster, A. R., Ji, L., Smith, R. K., & Brickhouse, N. S. 2012, ApJ, 756, 128
Fruscione, A., McDowell, J. C., Allen, G. E., et al. 2006, Proc. SPIE, 6270, 62701V
Gabriel, A. H., & Jordan, C. 1969, MNRAS, 145, 241
Gayley, K. G. 2016, AdSpR, 58, 719
Gottlieb, E. W., & Liller, W. 1978, ApJ, 225, 488
Gräfener, G., & Hamann, W.-R. 2005, A&A, 432, 633
Gräfener, G., Koesterke, L., & Hamann, W.-R. 2002, A&A, 387, 244
Gredel, R., Black, J. H., & Yan, M. 2001, A&A, 375, 553
Hamann, W.-R., & Gräfener, G. 2004, A&A, 427, 697
Hamann, W.-R., & Koesterke, L. 1998, A&A, 335, 1003
Harnden, F. R., Jr., Branduardi, G., Gorenstein, P., et al. 1979, ApJL, 234, L51
Henley, D. B., Corcoran, M. F., Pittard, J. M., et al. 2008, ApJ, 680, 705
Henley, D. B., Stevens, I. R., & Pittard, J. M. 2005, MNRAS, 356, 1308
Hervé, A., Rauw, G., & Nazé, Y. 2013, A&A, 551, A83
Hillier, D. J., Davidson, K., Ishibashi, K., & Gull, T. 2001, ApJ, 553, 837
Houck, J. C., & Denicola, L. A. 2000, in ASP Conf. Ser. 216, Astronomical Data Analysis Software and Systems IX, ed. N. Manset, C. Veillet, & D. Crabtree (San Francisco, CA: ASP), 591
Huenemoerder, D. P., Gayley, K. G., Hamann, W.-R., et al. 2015, ApJ, 815, 29
Humphreys, R. M., & Davidson, K. 1979, ApJ, 232, 409
Ignace, R. 2001, ApJL, 549, L119
Ignace, R., Gayley, K. G., Hamann, W.-R., et al. 2013, ApJ, 775, 29
Ignace, R., Oskinova, L. M., & Foullon, C. 2000, MNRAS, 318, 214
Kaper, L., van der Meer, A., & Najarro, F. 2006, A&A, 457, 595
Kitamoto, S., & Mukai, K. 1996, PASJ, 48, 813
Klochkova, V. G., & Chentsov, E. L. 2004, ARep, 48, 1005
Kobulnicky, H. A., Smullen, R. A., Kiminki, D. C., et al. 2012, ApJ, 756, 50

Langer, N. 2012, ARA&A, 50, 107
Laur, J., Tuvikene, T., Eenmäe, T., Kolka, I., & Leedjärv, L. 2012, BaltA, 21, 531
Leutenegger, M. A., Owocki, S. P., Kahn, S. M., & Paerels, F. B. S. 2007, ApJ, 659, 642
Lucy, L. B., & White, R. L. 1980, ApJ, 241, 300
Luehrs, S. 1997, PASP, 109, 504
Macfarlane, J. J., Cassinelli, J. P., Welsh, B. Y., et al. 1991, ApJ, 380, 564
Maíz Apellániz, J., Sota, A., Arias, J. I., et al. 2016, ApJS, 224, 4
Maryeva, O. V., Chentsov, E. L., Goranskij, V. P., et al. 2016, MNRAS, 458, 491
Massa, D., Oskinova, L., Fullerton, A. W., et al. 2014, MNRAS, 441, 2173
Morford, J. C., Fenech, D. M., Prinja, R. K., Blomme, R., & Yates, J. A. 2016, MNRAS, 463, 763
Naoz, S., & Fabrycky, D. C. 2014, ApJ, 793, 137
Nazé, Y., Oskinova, L. M., & Gosset, E. 2013, ApJ, 763, 143
Nazé, Y., Rauw, G., & Hutsemékers, D. 2012, A&A, 538, A47
Oskinova, L. M. 2005, MNRAS, 361, 679
Oskinova, L. M. 2016, AdSpR, 58, 739
Oskinova, L. M., Clarke, D., & Pollock, A. M. T. 2001, A&A, 378, L21
Oskinova, L. M., Feldmeier, A., & Hamann, W.-R. 2006, MNRAS, 372, 313
Oskinova, L. M., Gayley, K. G., Hamann, W.-R., et al. 2012, ApJL, 747, L25
Oskinova, L. M., Hamann, W.-R., Feldmeier, A., Ignace, R., & Chu, Y.-H. 2009, ApJL, 693, L44
Owocki, S. P., & Cohen, D. H. 2001, ApJ, 559, 1108
Pallavicini, R., Golub, L., Rosner, R., et al. 1981, ApJ, 248, 279
Parkin, E. R., Pittard, J. M., Corcoran, M. F., & Hamaguchi, K. 2011, ApJ, 726, 105
Pittard, J. M. 2009, MNRAS, 396, 1743
Podsiadlowski, P., Joss, P. C., & Hsu, J. J. L. 1992, ApJ, 391, 246
Pollock, A. M. T., Corcoran, M. F., Stevens, I. R., & Williams, P. M. 2005, ApJ, 629, 482
Porquet, D., & Dubau, J. 2000, A&AS, 143, 495
Porquet, D., Mewe, R., Dubau, J., Raassen, A. J. J., & Kaastra, J. S. 2001, A&A, 376, 1113
Puebla, R. E., Hillier, D. J., Zsargó, J., Cohen, D. H., & Leutenegger, M. A. 2016, MNRAS, 456, 2907
Quataert, E., Fernández, R., Kasen, D., Klion, H., & Paxton, B. 2016, MNRAS, 458, 1214
Rauw, G. 2011, A&A, 536, A31
Rauw, G., & Nazé, Y. 2016, AdSpR, 58, 761
Rauw, G., Nazé, Y., Wright, N. J., et al. 2015, ApJS, 221, 1
Salas, J., Maíz Apellániz, J., & Barbá, R. H. 2015, in Proc. of the XI Scientific Meeting of the Spanish Astronomical Society, Highlights of Spanish Astrophysics VIII, ed. A. J. Cenarro et al. (Berlin: Springer), 615
Sana, H., de Mink, S. E., de Koter, A., et al. 2012, Sci, 337, 444
Sander, A., Shenar, T., Hainich, R., et al. 2015, A&A, 577, A13
Sanyal, D., Grassitelli, L., Langer, N., & Bestenlehner, J. M. 2015, A&A, 580, A20
Scuderi, S., Panagia, N., Stanghellini, C., Trigilio, C., & Umana, G. 1998, A&A, 332, 251
Shaviv, N. J. 2000, ApJL, 532, L137
Shenar, T., Oskinova, L., Hamann, W.-R., et al. 2015, ApJ, 809, 135
Smith, R. K., Brickhouse, N. S., Liedahl, D. A., & Raymond, J. C. 2001, ApJL, 556, L91
Souza, S. P., & Lutz, B. L. 1980, ApJL, 235, L87
Steinke, M., Oskinova, L. M., Hamann, W.-R., et al. 2016, A&A, 588, A9
Stevens, I. R., Blondin, J. M., & Pollock, A. M. T. 1992, ApJ, 386, 265
Toalá, J. A., Guerrero, M. A., Ramos-Larios, G., & Guzmán, V. 2015, A&A, 578, A66
Todt, H., Sander, A., Hainich, R., et al. 2015, A&A, 579, A75
Vanbeveren, D., De Loore, C., & Van Rensbergen, W. 1998, A&ARv, 9, 63
Vishniac, E. T. 1994, ApJ, 428, 186
Waldron, W. L., & Cassinelli, J. P. 2007, ApJ, 668, 456
Waldron, W. L., Corcoran, M. F., Drake, S. A., & Smale, A. P. 1998, ApJS, 118, 217
Whittet, D. C. B. 2015, ApJ, 811, 110